Island scanning pattern optimization for residual deformation mitigation in laser powder bed fusion via sequential inherent strain method and sensitivity analysis

Qian Chen [a], Hunter Taylor [b], Akihiro Takezawa [c], Xuan Liang [a], Xavier Jimenez [a], Ryan Wicker [b], Albert C. To [a,*]

[a] Department of Mechanical Engineering and Materials Science, University of Pittsburgh, Pittsburgh, PA 15261, United States
[b] Department of Mechanical Engineering, University of Texas at El Paso, El Paso, TX 79968, United States
[c] Department of Applied Mechanics and Aerospace Engineering, Waseda University, Tokyo 169-8555, Japan

A B S T R A C T

Laser powder bed fusion (L-PBF) has emerged as one of the mainstream additive manufacturing approaches for fabricating metal parts with complex geometries and intricate internal structures. However, large deformation associated with rapid heating and cooling can lead to build failure and requires post-processing which may increase manufacturing cost and prolong the production period. In this work, an island scanning pattern design method is proposed to optimize the scanning direction of each island in order to reduce part deformation after cutting off the build platform. The objective of this optimization is to minimize the upward bending of the part after sectioning, which allows the part deformation to satisfy the tolerance requirement or reduce the post heat treatment time. Inherent strain method is employed in the sequential finite element analysis consisting of layer-by-layer activations and sectioning for fast residual distortion prediction. Full sequential sensitivity analysis for the formulated optimization is provided to update the island scanning directions. To show the feasibility and effectiveness of the proposed method, the scanning patterns of a block structure and a connecting rod were designed and parts were fabricated using an open architecture L-PBF machine. The fabrication experiments demonstrated that the residual deformation of both parts fabricated by optimized scanning pattern can be reduced by over 50% compared to the initial scanning patterns, which demonstrate the effectiveness of the proposed method.

1. Introduction

Powder bed fusion (PBF) processes, including laser powder bed fusion (L-PBF) and electron beam powder bed fusion (EB-PBF) are commonly used metal additive manufacturing (AM) techniques for fabricating near fully-dense metal components with complex geometry and intricate internal structures. Metal parts are built in a layer-by-layer fashion by laser or electron beam with diameter size of tens of microns, which leads to high build accuracy and surface finish. Powder bed fusion has been extensively used in industry to manufacture parts such as turbine blades with internal cooling channels, combustion chamber nozzles, and biomedical implants with intricate lattice structures. However, manufacturing defects such as internal voids [1,2] and un-desired grain structure [3] are still major issues in additive

manufacturing. Besides these defects, residual stress induced by the high temperature gradient near the laser beam and rapid heating and cooling leads to manufacturability issues such as cracking, warpage, and delamination during processing and may result in build failures [4–7] as shown in Fig. 1. Parts can also exhibit large deformation after removal from the building platform due to stress relief which is detrimental to mechanical performance [8,9], dimensional accuracy [10], and fatigue life [11–13]. In order to mitigate residual stress and deformation, post heat treatment [14] is often required which takes several hours or even days and increases the overall manufacturing costs [15].

Kruth et al. [17] found that shorter scan vectors could decrease residual stress in their experiment with Ti-6Al-4V selective laser melting (SLM). Similarly, island scanning strategy, a patent held by Concept Laser, divides each layer into islands forming a chessboard pattern,
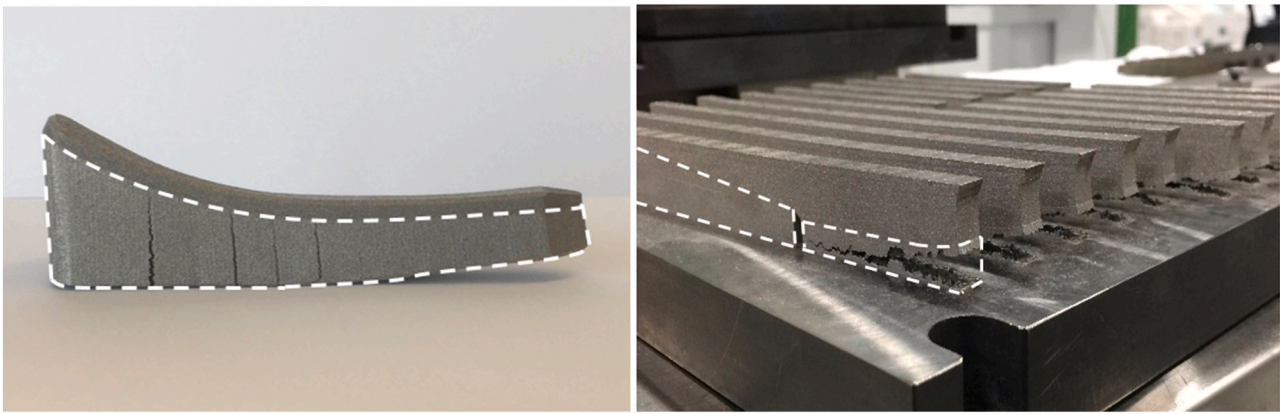
Fig. 1. Build failures of metal AM: (a) large residual deformation; (b) cracking due to residual stress [16].

where each island is raster scanned with shorter scan tracks. It has been reported that island scanning strategy can effectively decrease residual stress and cracks in EB-PBF [18]. Island scanning strategy has also been employed by commercial metal AM systems such as Renishaw AM500, Arcam Q20 and AconityOne, the last of which is used in this study. Kruth et al. [19] conducted experiments to study the effect of island scanning strategy on residual stress in SLM processed Ti-6Al-4V. It has been confirmed that island scanning strategy could reduce residual stress and the maximum reduction is achieved when rotating the island 45° with respect to the island edge and each island is filled hatch lines parallel to the island edge. It has also been reported that changing island size does not give any further contributions. Lu et al. [20] studied the microstructure, mechanical properties, and residual stress of Inconel 718 parts manufactured by SLM with different island size. It has been reported that enlarging the island size leads to higher density while the smallest island size leads to lowest residual stress, which is attributed to stress release from cracking. Cheng et al. [21] compared the residual deformation and stress of different scanning strategies and confirmed the effect of island scanning strategy on residual deformation and stress reduction. Thijs et al. [22] studied the influence of varying laser path, unidirectional and bidirectional, and rotating scanning direction layer-wise on microstructure and texture of parts fabricated by Concept Laser M1. In above studies, the vectors in neighboring islands are set to be perpendicular to each other in the build empirically. In this work, the scan vector orientations will be optimized to further reduce residual deformation.

There are few works on scanning pattern and path design for metal AM to reduce residual stress and distortion. For commercial powder bed fusion systems, besides island scanning strategy, another commonly used scan configuration is the stripe pattern (e.g., employed by EOS M290 DMLS), which divides each layer into a few bands with overlap between neighboring stripes. To the best of the authors' knowledge, key parameters including hatch spacing, rotating angle, stripe width and stripe overlap in these scanning patterns are determined by trial and error while scanning directions are rotated by a constant angle. Liang et al. [23] compared the effect of different popular laser scanning strategies including parallel line scanning, rotating angles and island scanning on residual deformation of the L-PBF metal parts. Chen et al. [24] proposed a continuous scanning path optimization method based on level-set to reduce the residual deformation and stress that can be used in wire feed or directed energy deposition (DED) process. Ding et al. [25, 26] proposed a continuous path planning method based on medial axis transformation algorithm to produce void- and gap-free part in wire + arc additive manufacturing (WAAM). The main obstacles existing in metal AM scanning pattern optimization are: (1) High computation cost of full-scale process simulation; (2) Difficulty in quantifying the effect of scanning vector on residual deformation and stress.

Even though scanning pattern optimization for metal AM is not well

developed, deposition path planning for polymer and fiber AM process such as fused filament fabrication (FFF) has been extensively studied, wherein the material properties are greatly affected by the build direction. Deposition path is taken as a scattered design variable [27–29] or continuous level-set function [30–32] in the design. Hoglund [27] proposed continuous fiber angle optimization approach for fiber-reinforced polymer printing. Fiber angles are treated as discrete variables without considering the overall path continuity in this work. Xia et al. [28] improved the spatial continuity of fiber angle by Shepard interpolation in composite structure optimization with scattered design variables. Kiyono et al. [29] proposed a fiber path optimization method based on normal distribution function and introduced filters with different radius to control the fiber continuity. Other than these designs with scattered variables, fiber deposition path can also be represented by level-set functions, and the inherent feature of this method guarantees continuity of the optimized paths all the time. In addition to fiber deposition and polymer printing, the level set method has been applied to contour-offset path generation for traditional machining [33,34] as well. Among the aforementioned methods, the approaches developed with scattered variables will be referred in this paper to define the scan track orientation of islands as scattered design variables.

This paper proposes a method to optimize the scanning pattern for the island scanning strategy of L-PBF for the purpose of reducing deformation of fabricated parts after their removal from the build substrate. The remaining content of this paper is organized as follows. In Section 2, the framework of scanning pattern optimization for powder bed fusion process is presented including the modified inherent strain method, formulation of the optimization algorithm, and sensitivity analysis for design variable update. In Section 3, we present the scanning pattern design for a simple block structure and a complex connecting rod with experimental validation. In Section 4, conclusions about the proposed scanning pattern design are given.

2. Island pattern design method

The island scanning strategy employed in most real applications usually uses hatch lines parallel to the island edge and keeps the scanning vector in the neighboring island perpendicular to each other. This strategy is not optimal according to the given geometry and may lead to large residual deformation for some parts. In the proposed island scanning pattern design method, the scanning direction of each island in a given geometry is taken as a design variable. An optimal scanning direction for each island is obtained from an iterative optimization algorithm via finite element analysis. Through optimizing the laser scanning direction in each island, the residual deformation of part after cutting off from build platform can be reduced significantly.
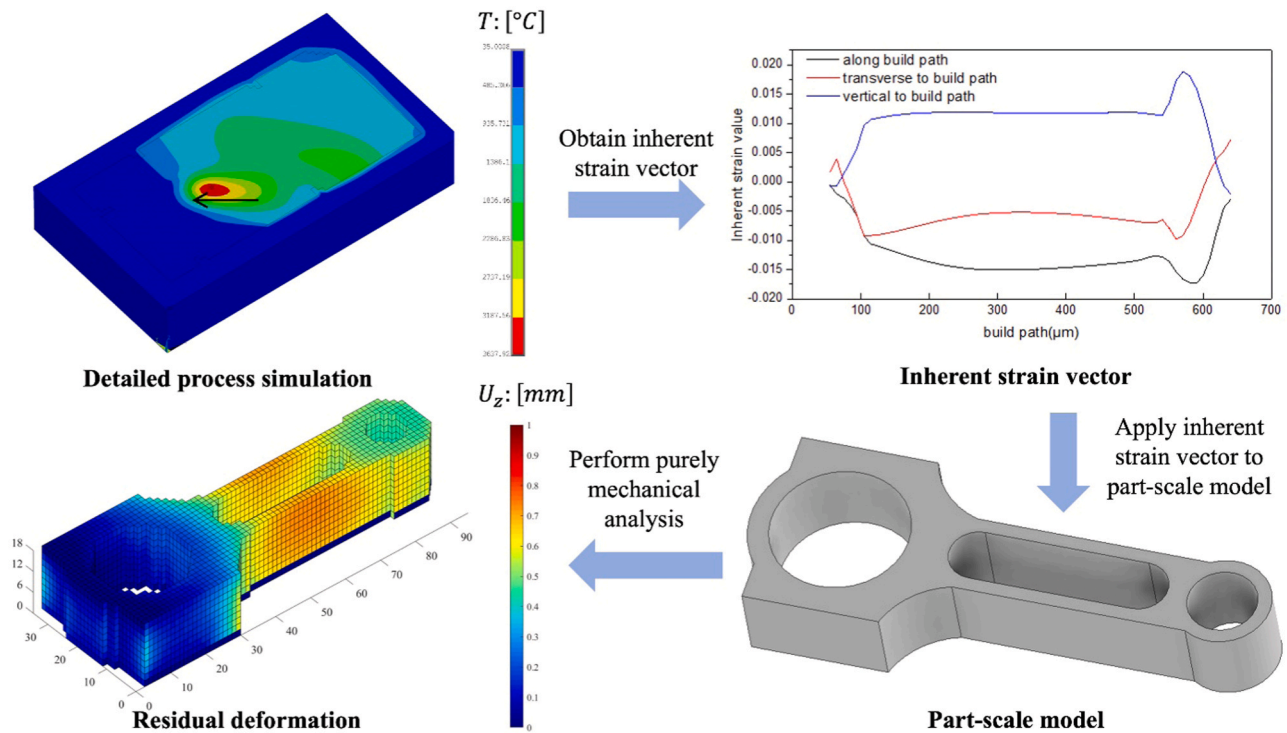
Fig. 2. Workflow of the modified inherent strain method [45].

2.1. Modified inherent strain method

Residual stress and deformation are among the most common issues in metal AM which have been extensively studied. The underlying mechanism is that powder particles are melted by the moving laser or electron beam and the molten material tends to expand due to rapid heating. This thermal expansion is restrained by neighboring solidified material or substrate which in turn leads to accumulation of negative plastic strain because both yield strength and Young's modulus of the solidified material are extremely low at elevated temperature. The material then undergoes rapid cooling due to heat sink, convection and radiation, and tends to contract. This contraction is also constrained by surrounding depositions and substrate and gives rise to tensile strain. In metal AM processes such as powder bed fusion, a part is built in a layer-by-layer fashion, and the deposition layer would be remelted several times due to subsequent layer deposition, where re-melting can partially relieve the tensile strain. The shrinkage from subsequent layers could even turn the stress in the middle of the building part into compressive. Boundary conditions also play an important role in residual stress and deformation. Building platform or substrate, which is much larger than the fabricated part, can give strong constraint to prevent contraction of bottom layers to acquire large tensile stress. The accumulation and evolution of residual stress through the entire build process finally leads to residual deformation.

Although thermomechanical models at different scale have been established and calibrated for residual stress and distortion prediction in metal AM [5,35–40], part-scale process simulation is still very computationally expensive and time-consuming. For gradient-based iterative optimization, it is impractical to perform detailed thermomechanical simulations iteratively, each of which may take a few hours even for a simple geometry. As an alternative to detailed simulation at part-scale, the so-called inherent strain method, which was originally proposed for welding simulation [41–43], is adopted in this work to address the high computational cost issue. The inherent strain method shortens part-scale deformation simulation to a few minutes in each iteration while having less than 10% prediction error. In particular, the key idea

behind the modified inherent strain method is to compute the inherent strain vector from the elastic and plastic strain histories in a pre-run detailed process simulation (based on moving point heat source model) and then apply the inherent strain vector as thermal expansion coefficients on the part in a series of layer-by-layer static equilibrium analyses [44,45]. The shrinkage of the solidified material due to the complex mechanics associated with rapid heating and cooling is introduced by giving a unit temperature rise in the part-scale simulation. The modified inherent strain method avoids the expensive detailed thermomechanical analysis with fine mesh resolution and lots of time steps to yield a relatively accurate deformation profile (see Fig. 2).

The basic procedures of the modified inherent strain method employed in this work to compute deformation profile are:

1) A detailed process simulation is performed on a micro-scale model to obtain the inherent strain vector which considers the inherent deformation introduced by laser melting and solidification.
2) The obtained inherent strain vector is then applied as coefficients of thermal expansion (CTE) to part-scale model for residual deformation prediction.

Besides part-scale residual stress and distortion in metal AM, the modified inherent strain method has been applied to the prediction of cracking [46,47], design of support structures [16] build orientation optimization [48] and continuous scanning path [24]. In these above studies, inherent strain is applied to the part in "one shot", which means the inherent strain vectors are not applied layer by layer but to the entire part at the same time. In this work, we propose a method to simulate the layer-wise building process with inherent strain vector. Details regarding the corresponding finite element method and sensitivity analysis will be given in Sections 2.2 and 2.3, respectively. The material of interest in the design and experimental validation is Ti6Al4V and the basis inherent strain vector (i.e., scanning track is horizontal: $0°$ and $180°$) used is: $[-0.02, \ -0.01, \ 0.015]$ (ε_{xx}, ε_{yy} and ε_{zz}) which is extracted from thermomechanical simulation for a single track, see Ref. [45] for details. The transformation rule of scan orientation
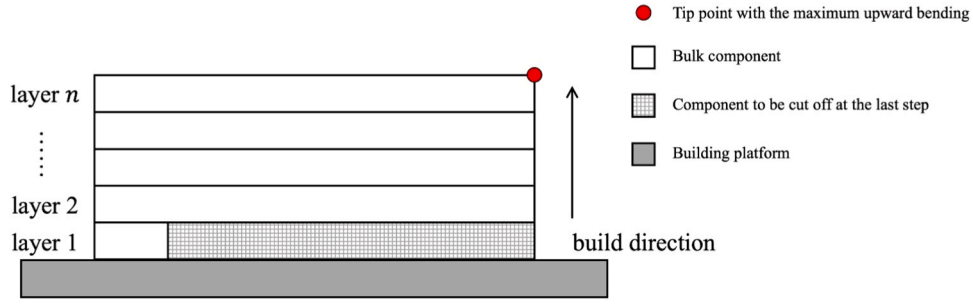
○ Tip point with the maximum upward bending

□ Bulk component

▦ Component to be cut off at the last step

▨ Building platform

Fig. 3. Schematic of finite element analysis with layer-by-layer deposition and subsequent sectioning.

dependent inherent strain vector will be discussed in Section 2.2.

2.2. Reformulation of governing equations

In the optimization, elastic finite element analysis with multiple time steps including the layer-wise deposition and cutting off in the last step is conducted iteratively to compute the part deformation. The schematic for the finite element analysis is shown in Fig. 3: (1) The part is sliced into n layers and is activated layer-by-layer from the bottom to top layers to model the material deposition; (2) One more time step, step $n + 1$, corresponding to cutting off from the large build platform for stress relief is carried out once the building simulation for the entire part is done. In every iteration, the finite element analysis for deformation prediction has $n+1$ time steps in total, and the equilibrium equations corresponding to the activation from layer 1 to n can be expressed as:

$$\mathbf{K}_1\mathbf{U}_1 = \mathbf{f}_1 \tag{1 -1}$$

$$\mathbf{K}_2\mathbf{U}_2 = \mathbf{K}_1\mathbf{U}_1 + (\mathbf{K}_2 - \mathbf{K}_1)\mathbf{U}_1 + \mathbf{f}_2 \tag{1 -2}$$

$$\mathbf{K}_n\mathbf{U}_n = \mathbf{K}_{n-1}\mathbf{U}_{n-1} + (\mathbf{K}_n - \mathbf{K}_{n-1})\mathbf{U}_{n-1} + \mathbf{f}_n \tag{1 -n}$$

where $\mathbf{K}_i$, $\mathbf{U}_i$ and $\mathbf{f}_i$ are the stiffness matrix, the displacement vector, and the force vector associated with scanning orientation dependent inherent strain vector for layer i. On the right-hand-side of Eqs. (1–2 to 1-n), the first term is the force vector from the previous layer; the second term is the load increment needed to keep the displacement unchanged when activating the new layer; the third term, $\mathbf{f}_k$, is the force due to deformation induced by deposition of layer k and can be expressed as a function of the inherent strain vector:

$$\mathbf{f}_k = \sum_{i \in ele\_act_k} \int_{\Omega_i} \mathbf{B}_e^T \mathbf{C}\boldsymbol{\varepsilon}(\theta_i) d\Omega \tag{2}$$

where $\mathbf{B}_e^T$ is the strain-displacement matrix, $\mathbf{C}$ is the element elasticity matrix, and $\boldsymbol{\varepsilon}(\theta_i)$ is the inherent strain vector as a function of the scanning orientation. In this work, we assume only the strain components within xy plane are dependent on the scanning orientation while the strain vector along the building direction ε_z is constant. According to the classic solid mechanics theory, the plane strain transformation with respect to θ is performed as following:

$$\varepsilon_{xx}(\theta) = \frac{\varepsilon_x + \varepsilon_y}{2} + \frac{\varepsilon_x - \varepsilon_y}{2}cos(2\theta) + \varepsilon_{xy}sin(2\theta) \tag{3 -1}$$

$$\varepsilon_{yy}(\theta) = \frac{\varepsilon_x + \varepsilon_y}{2} - \frac{\varepsilon_x - \varepsilon_y}{2}cos(2\theta) - \varepsilon_{xy}sin(2\theta) \tag{3 -2}$$

$$\varepsilon_{xy}(\theta) = -\frac{\varepsilon_x - \varepsilon_y}{2}sin(2\theta) + \varepsilon_{xy}cos(2\theta) \tag{3 -3}$$

The equilibrium equation at time step $n+1$ corresponding to the cutting off at last time step is:

$$(\mathbf{K}_n - \Delta\mathbf{K}_{cut})\mathbf{U}_{n+1} = \mathbf{K}_n\mathbf{U}_n - \sum_{i \in ele\_cut} \int_{\Omega_i} \mathbf{B}_e^T \mathbf{C}\boldsymbol{\varepsilon}(\theta_i)d\Omega \tag{4}$$

where $\Delta\mathbf{K}_{cut}$ is the assembled stiffness matrix corresponding to elements which are removed in the last time step. It should be noted that on the right-hand-side of Eq. (4), the thermal loading vector of these removed elements is subtracted as well.

For the ease of sensitivity analysis in Section 2.4, the above governing equations in Eqs. (1) and (4) are reformulated in a more generic format:

$$\mathbf{A}_i\mathbf{U}_i + \mathbf{B}_i\Delta\mathbf{U}_{i-1} = \mathbf{f}_i, \quad i = 1, 2, \cdots n + 1 \tag{5}$$

where $\Delta\mathbf{U}_i = \mathbf{U}_i - \mathbf{U}_{i-1}$ and $\mathbf{U}_0 = \mathbf{0}$, $\mathbf{B}_i = \mathbf{K}_i$ and $\mathbf{B}_{n+1} = \mathbf{K}_n$, $\mathbf{A}_i$ is in the form of:

$$\mathbf{A}_i = \left\{ \begin{array}{ll} -\Delta\mathbf{K}_{cut}, & i = n + 1 \\ \mathbf{0}, & otherwise \end{array} \right\} \tag{6}$$

2.3. Problem formulation

After partially cutting the part off the build platform, a cantilever beam forms and bends upward, resulting in its end tip point having the largest deformation. The goal of scanning pattern design is to minimize the upward bending after stress relief and thus the displacement along the build direction (z) of the tip point is selected as the objective to be minimized. Hence the optimization can be mathematically formulated as:

$$min. \quad U_{n+1}^m \tag{7}$$

$$w.r.t \quad \boldsymbol{\theta}$$

$$s.t. \quad \mathbf{A}_i\mathbf{U}_i + \mathbf{B}_i\Delta\mathbf{U}_{i-1} = \mathbf{f}_i, \quad i = 1, 2, ..., n + 1 \tag{8}$$

where U_{n+1}^m is the displacement along building direction of the selected end point at the last time step $n+1$ and superscript m is the corresponding degree of freedom (DOF) number. The design variable is the orientation of the scanning path in each island. It is worth to emphasize that in the optimization, it is the island scanning orientation to be updated instead of the element. Each island usually has several elements and the thermal loading applied to each island is identical. The displacement vector must satisfy the equilibrium equations formulated in Section 2.2 where the force vector is a function of the design variables.

2.4. Sequential sensitivity analysis

Sensitivity analysis is part of the topology optimization [49,50] to update the design variables. The sequential sensitivity analysis performed in Ref. 51 will be invoked in this section to obtain the sensitivities in order to update the design variables of our optimization problem. The Lagrangian is obtained from Eqs. (7) and (8) and defined as follows:

$$L = U_{n+1}^m + \sum_{i=1}^{n+1} \boldsymbol{\lambda}_i^T(\mathbf{A}_i\mathbf{U}_i + \mathbf{B}_i\Delta\mathbf{U}_{i-1} - \mathbf{f}_i) \tag{9}$$
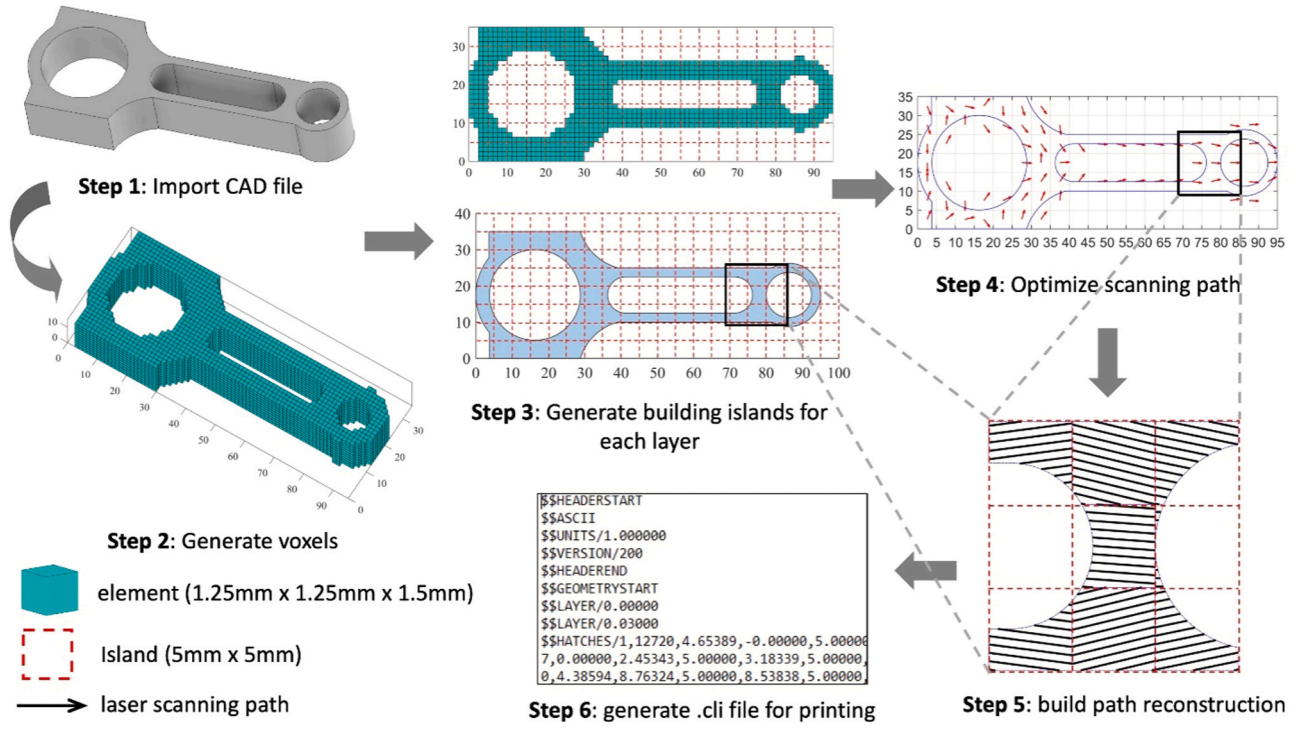
Fig. 4. Flowchart of island scanning pattern design.

where the first term is the displacement along the build direction (z) of the selected tip point; λ_i is the adjoint variable vector for step i; the second term of the Lagrangian is the summation of multiplication of equilibrium equation and corresponding adjoint variable at each time step.

Based on the chain rule, the derivative of the Lagrangian with respect to any design variable θ_k is obtained:

$$\frac{\partial L}{\partial \theta_k} = \frac{\partial U_{n+1}^m}{\partial \theta_k} + \sum_{i=1}^{n+1} \lambda_i^T \left(\mathbf{A}_i \frac{\partial \mathbf{U}_i}{\partial \theta_k} + \mathbf{B}_i \frac{\partial \Delta \mathbf{U}_{i-1}}{\partial \theta_k} - \frac{\partial \mathbf{f}_i}{\partial \theta_k} \right) \tag{10}$$

The first term on the right-hand-side of the above equation can be rewritten as:

$$\frac{\partial U_{N+1}^m}{\partial \theta_k} = \begin{bmatrix} 0 & \cdots & 0 & 1 & 0 & \cdots & 0 \end{bmatrix} \frac{\partial \mathbf{U}_{N+1}}{\partial \theta_k} = \mathbf{H}_{n+1} \frac{\partial \mathbf{U}_{N+1}}{\partial \theta_k} \tag{11}$$

where the $\mathbf{H}_{n+1}$ is a sparse vector and only the mth entry corresponding to the selected DOF adopts a value of unity. For the term associated with $\mathbf{B}_i \frac{\partial \Delta \mathbf{U}_{i-1}}{\partial \theta_k}$ in Eq. (10), recall that $\Delta \mathbf{U}_i = \mathbf{U}_i - \mathbf{U}_{i-1}$ and $\sum_{i=1}^n \Delta u_i v_i = u_{n+1} v_{n+1} - u_1 v_1 - \sum_{i=1}^n u_{i+1} \Delta v_i$, so we can expand all the terms as:

$$\sum_{i=1}^{N+1} \lambda_i^T \mathbf{B}_i \frac{\partial \Delta \mathbf{U}_{i-1}}{\partial \theta_k} = \lambda_{N+2}^T \mathbf{B}_{N+2} \frac{\partial \mathbf{U}_{N+1}}{\partial \theta_k} - \lambda_1^T \mathbf{B}_1 \frac{\partial \mathbf{U}_0}{\partial \theta_k}$$
$$- \sum_{i=1}^{N+1} \left(\Delta \lambda_i^T \mathbf{B}_{i+1} + \lambda_i^T \Delta \mathbf{B}_i \right) \frac{\partial \mathbf{U}_i}{\partial \theta_k} \tag{12}$$

According to Eqs. (10–12) and collecting the terms containing $\frac{\partial U_i}{\partial \theta_k}$, the adjoint variable vectors λ_i can be obtained by solving the following adjoint equations in a reverse direction from $n+1$ to 1:

$$\mathbf{H}_{n+1} + \lambda_{N+1}^T (\mathbf{A}_{N+1} + \mathbf{B}_{N+1}) = \mathbf{0} \tag{13}$$

$$\lambda_i^T (\mathbf{A}_i + \mathbf{B}_i) = \lambda_{i+1}^T \mathbf{B}_{i+1}, \quad i = N, N-1, \cdots 1 \tag{14}$$

Finally, the sensitivity given by the derivative of the Lagrangian can be obtained:

$$\frac{\partial L}{\partial \theta_k} = - \sum_{i=1}^{N+1} \lambda_i^T \frac{\partial \mathbf{f}_i}{\partial \theta_k} \tag{15}$$

2.5. Implementation steps

The flowchart of the island scanning pattern design method proposed in this study is summarized in Fig. 4. For any given geometry, the original CAD file is imported and the scanning pattern will then be designed in the following key steps:

- **Voxelization:** In Step 2, voxels are employed in this work to compute part deformation for the sake of mesh generation and computation efficiency. In voxelization, part of the local features of the imported geometry is lost but will be compensated when reconstructing the build path in Step 5.
- **Island discretization:** In Step 3, the voxels generated in the last step is sliced into layers by the building layer thickness; each layer is then discretized into islands of 5 mm × 5 mm square. The inherent strain vectors for elements in the same island are identical since the scanning track orientations are the same.
- **Scanning path optimization:** In Step 4, the design variable, scanning orientation of each island is updated iteratively until convergence. In every iteration, finite element analysis with multiple time steps is conducted to compute part deformation first and then sensitivities analysis derived in Section 2.4 is performed. All the element sensitivities in the same island will be grouped together to update the scanning orientation of each island.
- **Build path reconstruction:** In Step 5, scanning tracks within each island are determined by the optimized scanning orientation, hatch spacing and the interaction between island and local features. Although the resolution of the part used in finite element analysis is partially lost due to voxelization in Step 2, the build path reconstruction is based on the original geometry and the build file generated for manufacturing reserves all the features and resolutions.

Table 1
Processing parameters of AconityOne L-PBF systems for part fabrication.

Processing parameters	Values (units)
Island size	5 mm
Stripe overlap	0 mm
Skywriting	Yes
Power	250 W
Scan speed	1200 mm/s
Defocus	-2 mm
Spot size	0.08 mm
Hatch spacing	0.1 mm

3. Numerical examples and experimental validation

In this section, the scanning patterns for a block structure and a connecting rod are designed following the procedure for the proposed method in Fig. 4. The effectiveness of this method on deformation reduction will be experimentally validated. The scanning pattern design including voxelization, finite element analysis, sensitivity analysis, design variable update, build path reconstruction, and building file generation are implemented using MATLAB R2019a. All the parts with initial and designed scanning pattern are fabricated by an open-architecture L-PBF machine (details to be given below). The material used in the design and printing is Ti6Al4V, which has a Young's modulus of 104 GPa and Poisson's ratio of 0.34.

3.1. Experimental setup

The part manufacturing is performed on an AconityONE L-PBF system (Aconity3D, Aachen, Germany) equipped with a 1 kW Yb fiber laser (IPG Photonics, Oxford, MA, USA) and galvanometer scanning via 3D scanning optics (Raylase AxialScan-30, Wessling, Germany). The laser power is 250 W and the scan speed is 1200 mm/s with hatch spacing of 100 μm. The layer thickness used in the build process is 30 μm, while in the design, 50 physical layers are merged as one layer. The focused spot size, d4σ is 59 μm ± 5 μm measured with a Beam Watch AM (Ophir-Spricon, LLC, North Logan, UT, USA). The 3D scanning optics allows for programmable beam defocus to alter the spot size at the build plate. The feature is set to 2 mm defocus for production of the plates resulting in d4σ ~ 80 μm. The oxygen is continuously monitored during processing and maintained below 500 ppm. Chamber pressure is maintained at

45 mbar, and an inert gas consumption is < 2.5 L/min during the build.

The layer thickness is 30 μm with a dosing factor of 1.8 which means the supply platform moves upward by 54 μm each layer. Powder spreading is performed with dual carbon fiber brushes attached to a rigid carrier with a 200 mm/s deposition velocity. All builds are performed with parts scanned from near exhaust towards the gas cross flow nozzle to minimize scanning of splatter. The processing parameters for the building of block structure and connecting rod are summarized in Table 1.

3.2. Block structure example

The first case is a rectangle block structure and the dimension of the block is $100 \times 50 \times 15$ mm^3. In the scan pattern optimization, 50 physical layers are merged to save computation cost and the element size used in this case is $5 \times 5 \times 1.5$ mm^3. In this case, the element size is identical to the island. The finite element of the block is shown in Fig. 5 (a) which has 2000 elements and 2541 nodes. For each layer, the initial scan pattern is the same and as shown Fig. 5(b). Each island is filled with bi-directional hatch lines (0° and 180°) along the block long edge. After optimizing the scan pattern of each island, i.e., the hatch line direction, the maximum bending is expected to reduce after partially cutting off at the tip point as indicated in Fig. 5(a).

The optimization results are presented in Fig. 6 including the deformation profile after cutting off before and after scan pattern optimization. The figure also illustrates the optimized layer-wise scan pattern and the convergence history of the object function. As shown in Fig. 6(a), the upward bending after partially cutting off from the first layer is reduced significantly by optimizing the scan pattern for the block. The upward deformation along the center line after cutting off is plotted in Fig. 6(b). The deformation of the selected tip point on the top surface along the centerline is 8.4 mm before optimization and is reduced to 5.6 mm after optimization. The layer-wise scan pattern is presented in Fig. 6(c). It can be found that the global trend of optimized scan pattern direction is vertical, i.e., along the short edge of the block except the first layer. Since the block is partially cut from the substrate and only four islands along the long edge are kept, those islands cut off (indicated in the blue dashed line box in Fig. 6(c)) have two different parts in sensitivity analysis to update the island scan direction. For the sensitivities of these islands, the first contribution is from the first step to build the first layer, and the second part is from the last time step for cutting off, as shown in Eq. (15). The explanation for the optimized scan
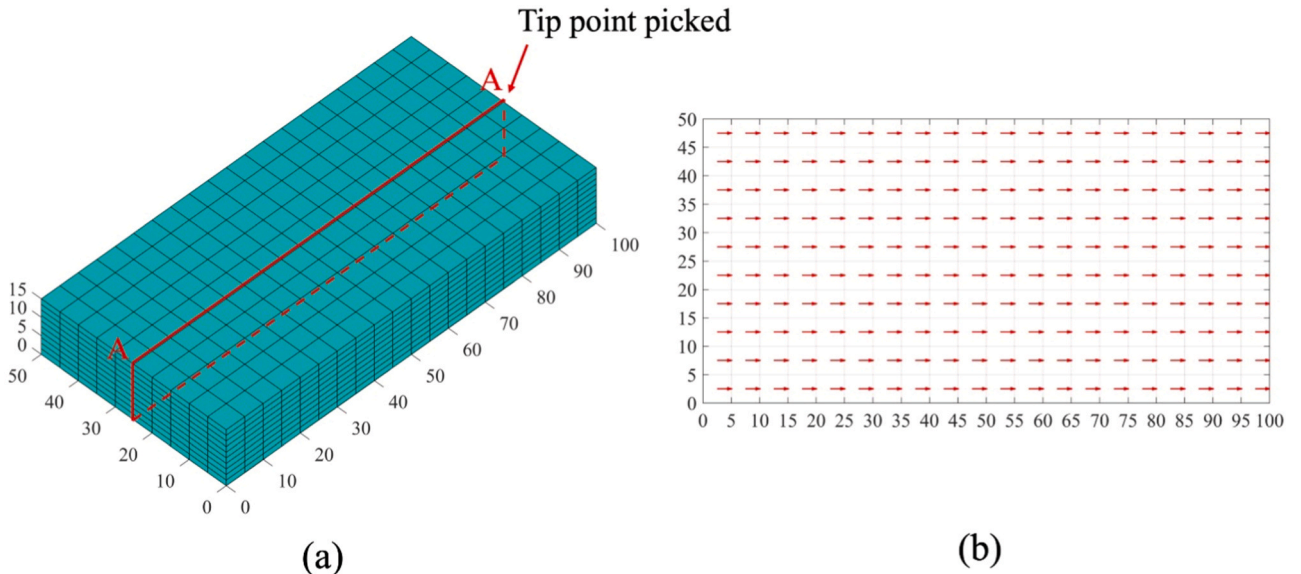

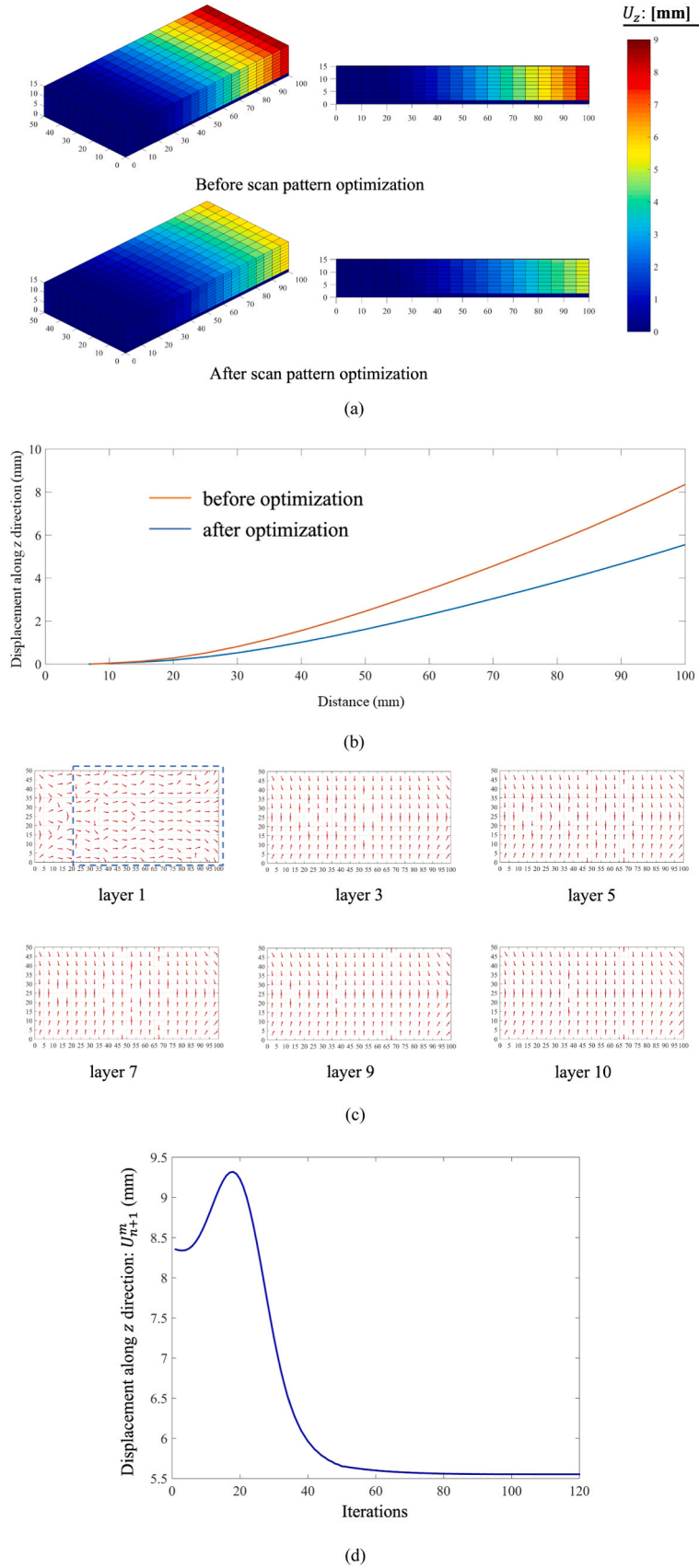**Fig. 5.** (a) Finite element model of the block structure; (b) Initial scan pattern for each layer.

Fig. 6. Optimized results for the block structure: (a) Deformation profile after cutting off; (b) Displacement along the center line on the top surface; (c) Layer-wise optimized scan pattern; (d) Convergence history. (For interpretation of the references to color in this figure legend, the reader is referred to the web version of this article.)
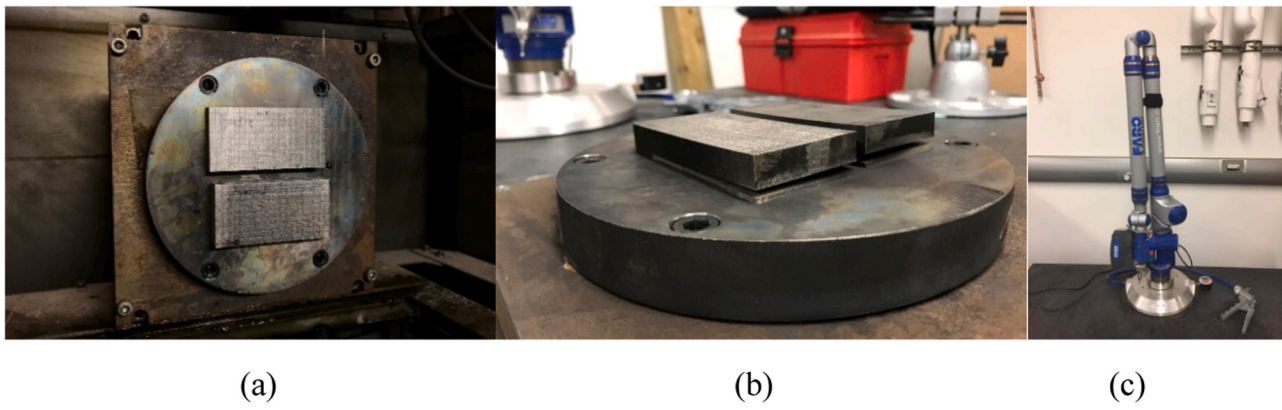
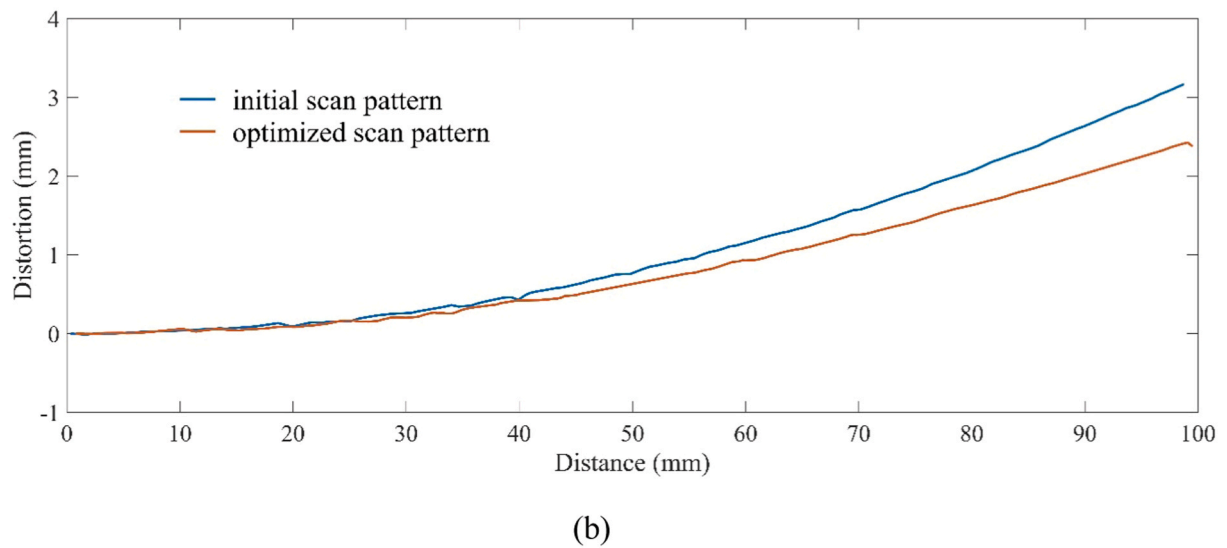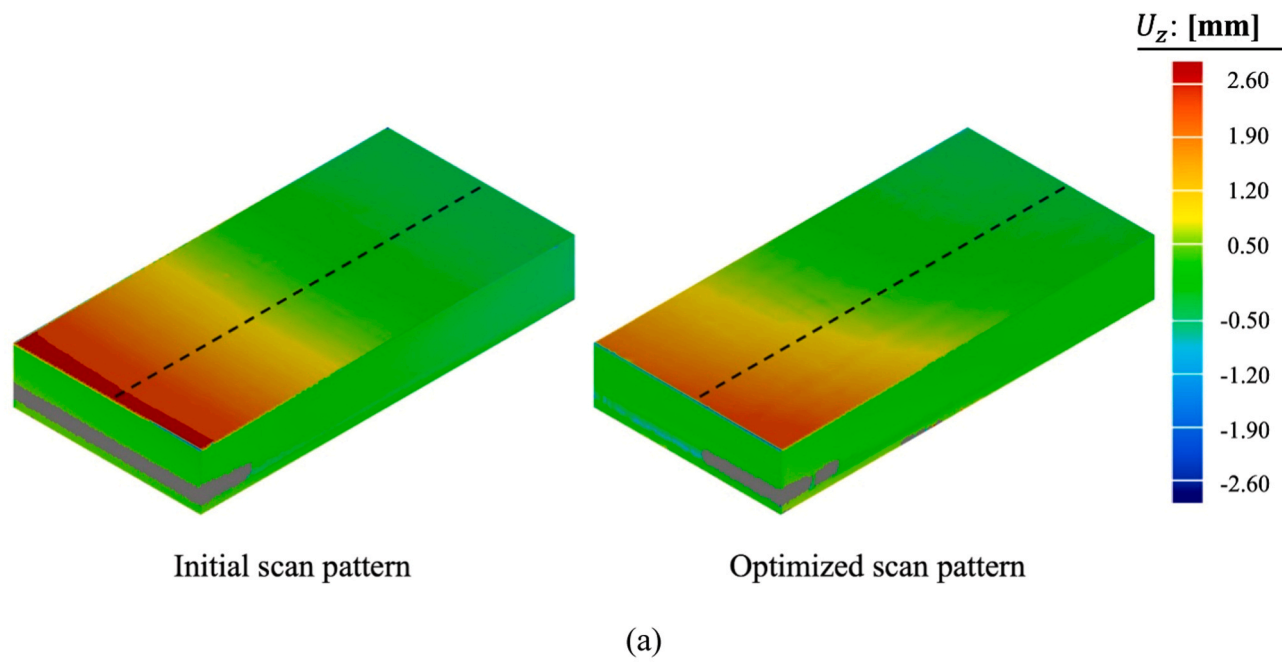**Fig. 7.** As-built block (a) before and (b) after stress relief; (c) Faro Laser ScanArm V3 for distortion measurement.

Fig. 8. Measured deformation comparison (a) Deformation profile; (b) Deformation along the black dashed line on the top surface.
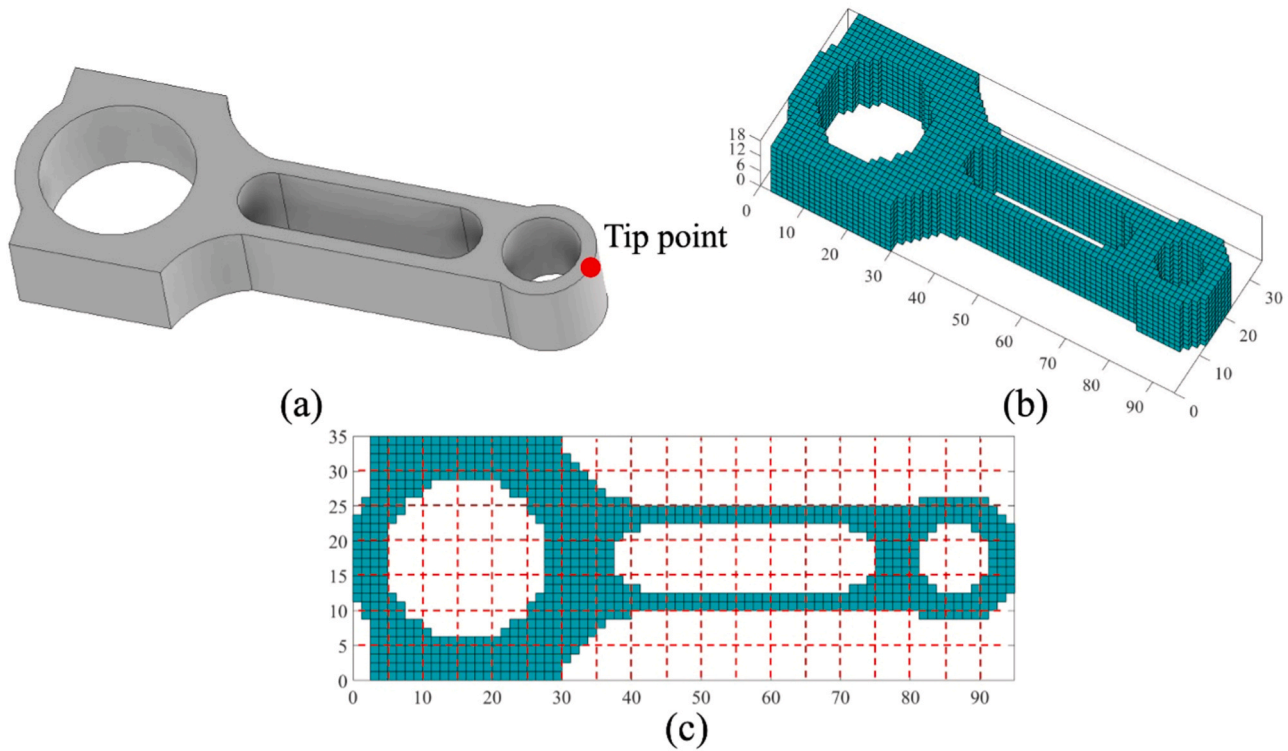
Fig. 9. (a) Imported connecting rod CAD model; (b) Voxelized finite element model; (c) Generated islands of each layer. (For interpretation of the references to color in this figure legend, the reader is referred to the web version of this article.)

pattern from layer 2 to layer 10 is as follows: The deformation is caused by the anisotropic shrinkage of material which shrinks more along the beam scanning direction and less along the transverse direction. With the initial scan pattern, the inherent strain vector applied is (−0.02, −0.01, 0.015) and the principal shrinkage direction is along the long edge direction which leads to large upward bending. After optimization, the global scan direction is almost vertical and makes the shrinkage along the long edge smaller.

To evaluate the performance of the optimized scan pattern, the same block structures were built on the same build platform by the initial scan pattern as indicated in Fig. 5(b) and optimized scan pattern in Fig. 6(c) for deformation measurement and comparison. As shown in Fig. 7, the as-built parts were partially cut from the platform (20 mm along the long edge is kept) by the electrical discharge machining (EDM), at a height of 1.5 mm, which equals to the element height. After stress relief, the deformation profile of two parts was measured by a Faro Laser ScanArm made by Faro Technologies. Further comparison between the original CAD file and measured deformation after cutting off was made by Geomagic Control X (3DSystems).

Fig. 8(a) presents the experimental measurement results for the blocks built by the initial and optimized scan pattern after cutting off, respectively. It can be found that both parts exhibit upward bending and have larger deformation near the left short top edge. The block with optimized scan pattern has smaller deformation than the block with initial scan pattern. Fig. 8(b) presents comparison of vertical displacement along the center line of the top surface, as indicated by the black dashed line in Fig. 8(a). The maximum deformation at the tip point is 3.2 mm for the block with initial scan pattern and 2.4 mm with the optimized scan pattern. This demonstrates the proposed scan pattern design method can significantly reduce the residual deformation, e.g., 23.41% in this case. It should be emphasized here that the experimentally measured residual deformation value is smaller than the predicted value in optimization. This deformation overestimation is attributed to the elastic finite element analysis performed in the optimization which neglects the plastic behavior. Despite not considering plasticity in the

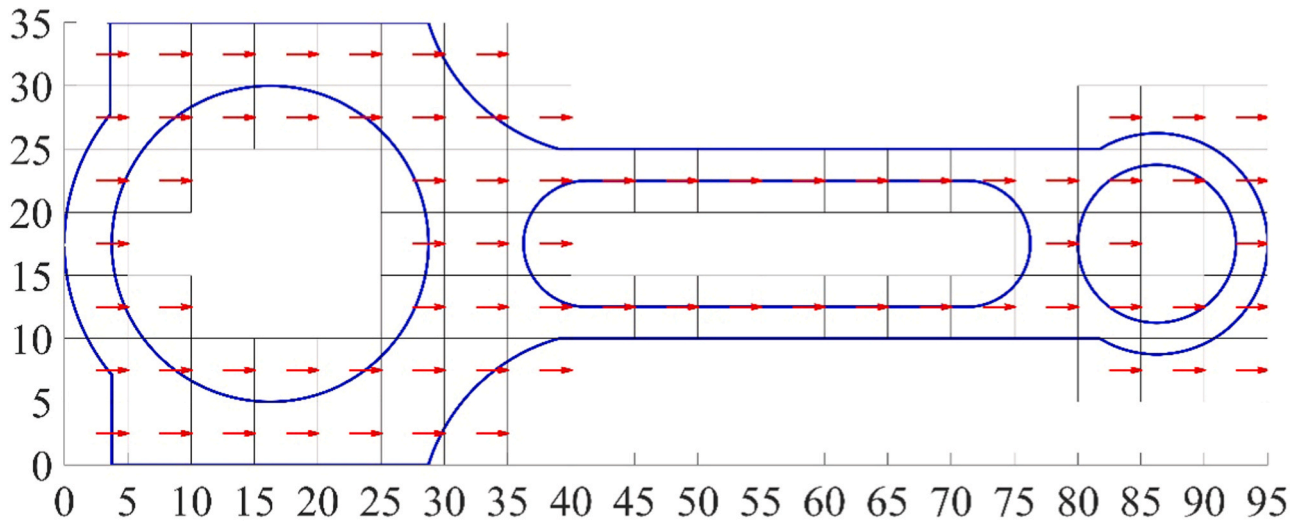optimization model, the optimized scan pattern still performs well.

3.3. Connecting rod example

The second case is a connecting rod and the dimension is $95 \times 35 \times 18$ mm^3, as shown in Fig. 9(a). In this case, 60 physical layers are merged as one layer and the part is voxelized with element size of $1.25 \times 1.25 \times 1.8$ mm^3. The finite element model of this connecting rod employed in scan pattern optimization is shown in Fig. 9(b), which has 21,280 elements and 24,563 nodes. The island size is 5×5 mm^2 in the build design. Each island is divided into 16 elements as shown in Fig. 9 (c).

The initial scan pattern is the same as the block structure case in Section 3.1. Each island is filled with bi-directional horizontal scan lines as shown in Fig. 10. Build path reconstruction is employed for each island depending on the intersection between island and geometry as shown in Fig. 10(b). The reconstructed build paths of initial scan pattern are used to build the connecting rod.

The optimized results for the connecting rod case are presented in Fig. 11 including the deformation profile after cutting off with initial and optimized scan pattern, layer-wised optimized scan pattern and reconstructed building path, and the convergence history. As shown in Fig. 11(a), the upward bending after partially cutting off the first layer is reduced significantly with optimized scan pattern compared to the deformation with initial scan pattern. The deformation of the selected tip point on the top surface along the center line, as indicated by the red dot in Fig. 9(a), is 0.83 mm before optimization and is reduced to 0.45 mm after optimization. The layer-wise scan pattern and reconstructed build path of layer 1, 3, 7 and 9 are presented in Fig. 11(b). The convergence history is presented in Fig. 11(c). The optimization converges with 80 iterations and takes 2.3 h to with Intel Xeon Gold 6136 3.0 GHz CPU (two processors) and 256GB RAM.

Different from the optimized scanning pattern of the block structure, which mainly consists of vertical scanning tracks, the optimized scanning pattern for connecting rod has islands with horizontal scanning

(a)
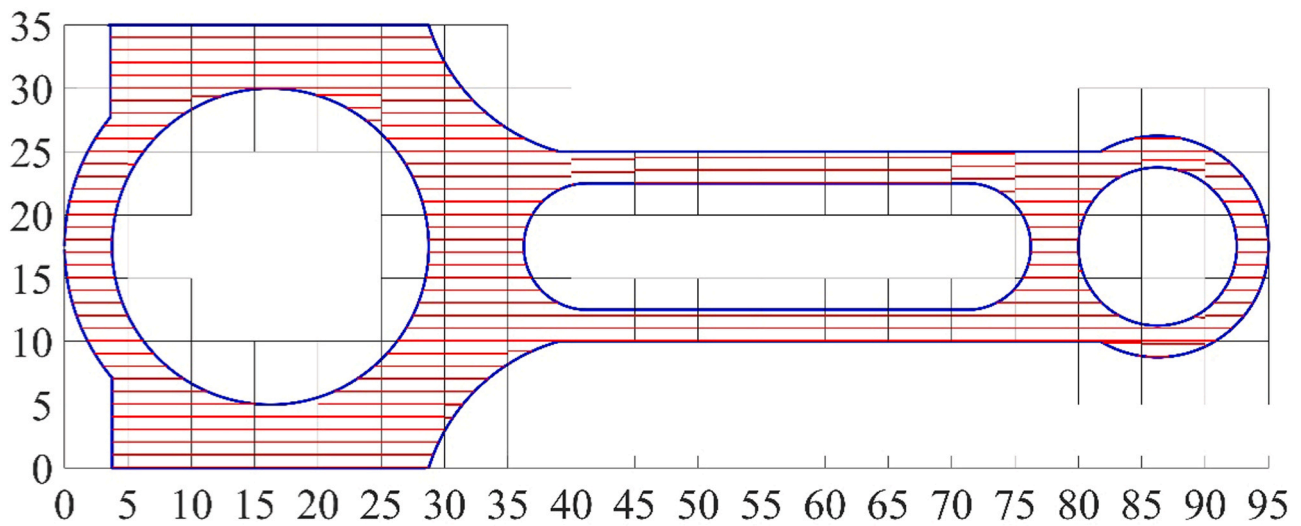
(b)

Fig. 10. (a) Initial scan pattern, (b) Build path reconstruction.

orientation near the small end and crank pin end (i.e. the large end) while the scanning orientation of the thin beams is vertical. Another feature of the optimized scanning pattern is that the island scanning orientation tends to fit the local geometry. For example, the scanning orientations of both large and small end varies along the tangential direction.

In Fig. 12, connecting rods with the initial parallel scanning pattern as indicated in Fig. 10 and optimized scanning pattern in Fig. 11(b) are built by the AconityOne system under the same process conditions as the block structure in Section 3.2. The as-built connecting rods were partially cut off from the tip by EDM at the height of 1.8 mm, which equals to one element height, and with 20 mm not cut off, which equals to the length of four islands.

The measured deformation profiles on the top surface of connecting rod with initial and optimized scanning pattern are presented in Fig. 13.

It can be found that the upward bending deformation after cutting off with initial scanning pattern is around two times larger than the deformation with optimized scanning pattern near the tip point. The deformation values of three picked points as indicated by the black dot near the small end are reduced by 55%, 52% and 53% from left to right after scanning pattern optimization. The effectiveness of the proposed scanning pattern optimization method on connecting rod structure is demonstrated through this comparison.

Besides the initial bi-directional horizontal scanning pattern in Fig. 10, and optimized scanning pattern in Fig. 11, the deformation profiles of the other two commonly used scanning pattern as indicated in Fig. 13 are computed for comparison. The first one is layer-wise rotation by 90°, and in the second one, the scanning directions in neighboring islands are orthogonal to each other while rotated by 90° layer-wise as shown in (Fig. 14).
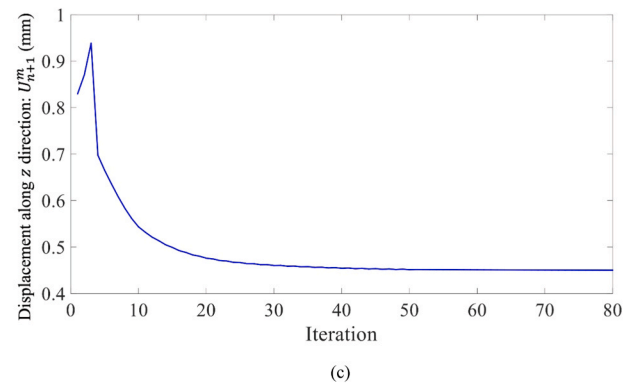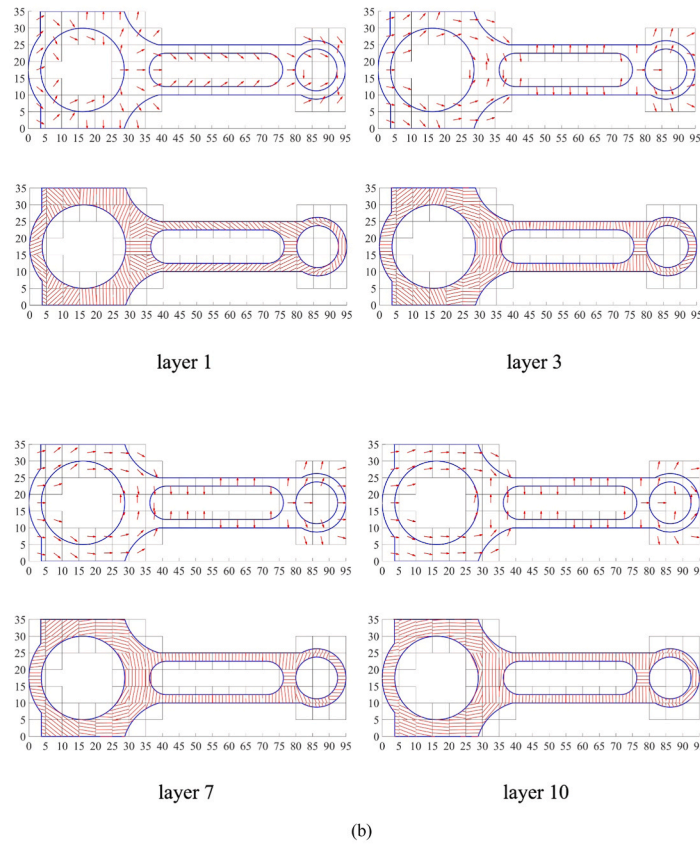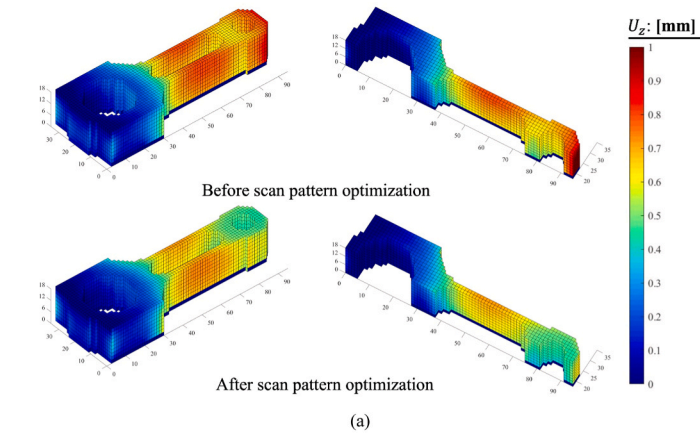
(a)

layer 1   layer 3

layer 7   layer 10

(b)

(c)

Fig. 11. Optimized results for the connecting rod: (a) Deformation profile after cutting off; (b) Layer-wise optimized scan pattern; (c) Convergence history.

Fig. 12. As-built connecting rods with initial and optimized scanning pattern: (a) before sectioning; (b) after sectioning.
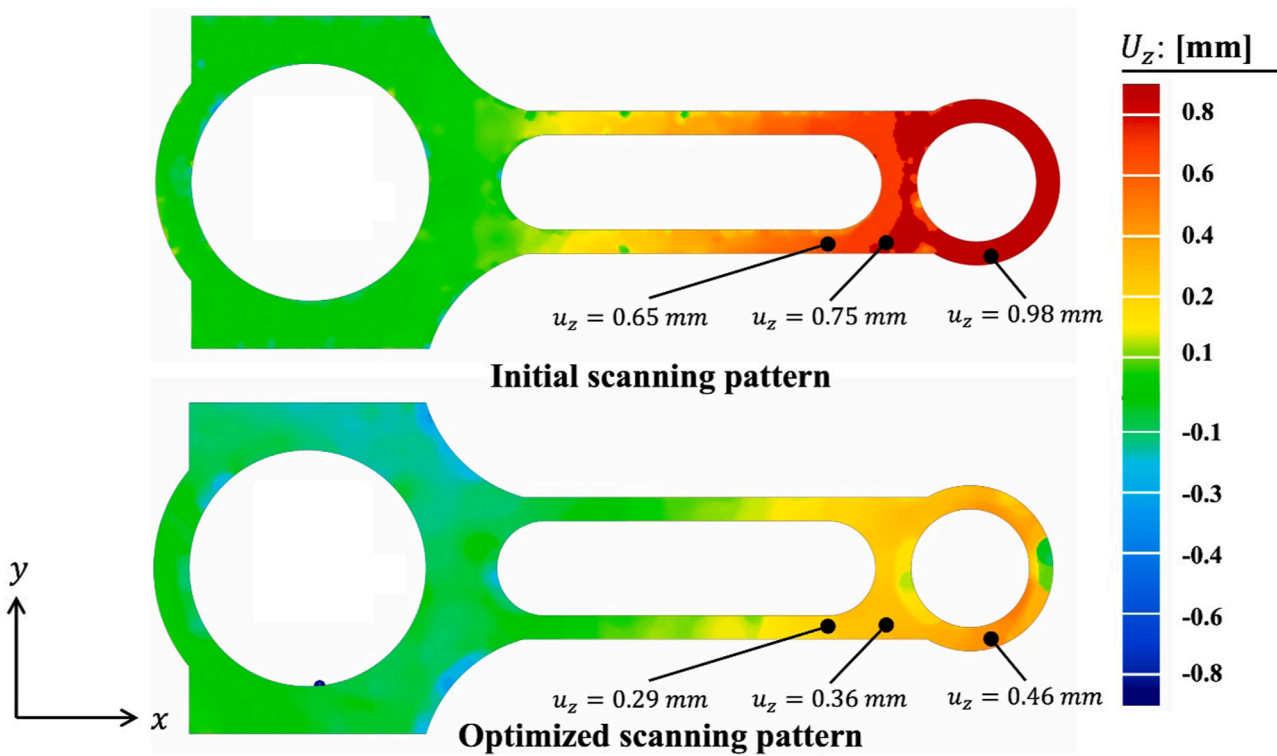

Fig. 13. Measured deformation profile on the top surface of connecting rods with initial and optimized scanning pattern.

The deformation profiles of the connecting rods with these two scanning patterns after cutting off are presented in Fig. 15. The deformation at the tip point with the layer-wise 90° rotation is much larger than that with scanning direction orthogonal to neighboring island scanning pattern. The comparison of deformation at the tip point between initial setup, these two commonly used scanning pattern and the optimized scanning pattern are listed in Table 2. It could be found that by rotating the scanning direction 90° layer-wise while keeping the scanning directions in neighboring islands could significantly reduce the residual deformation. Among all of these scanning patterns, the optimized one still has the best performance.

4. Conclusion

This work proposes a scan pattern design method for island scanning strategy to reduce part deformation encountered in powder bed fusion processing. Inherent strain depending on laser or electron beam scan orientation is employed to efficiently predict the deformation caused by powder particle melting and solidification. Part deformation is obtained from a multi-step static equilibrium analysis including layer-by-layer activation and cutting off at last step. Since post removal after building is considered in both finite element and sensitivity analysis, deformation of the as-built part after cutting off the build platform is minimized directly in the optimization. Important details of this
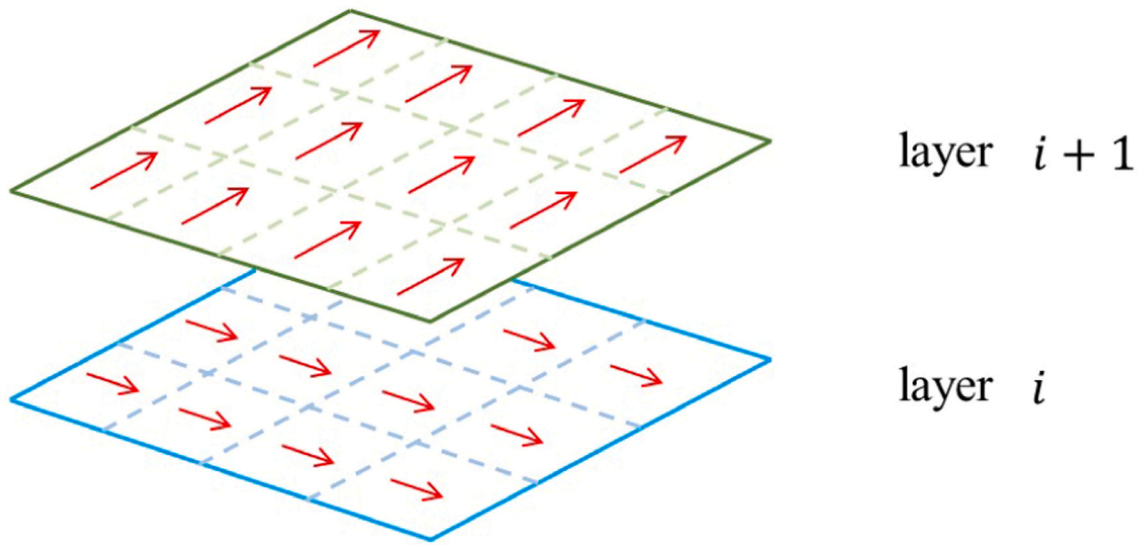
Layer-wise rotate by 90°

(a)
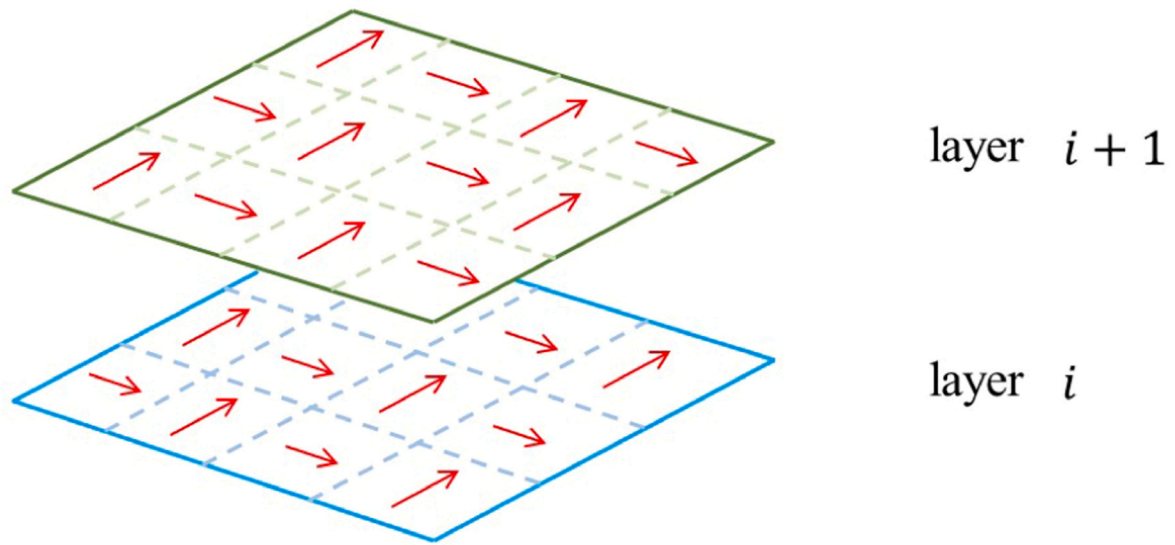
Scan direction of neighboring island orthogonal
to each other & layer-wise rotate by 90°

(b)

Fig. 14. Baseline scanning pattern (a) layer-wise 90° rotation and (b) neighboring island orthogonal and layer-wise 90° rotation.

proposed design method including voxelization, island discretization, optimization, and subsequent build path reconstruction are given in this paper. Two numerical examples are investigated to examine the performance of the proposed method. Experimental validations for the designed patterns are conducted on an open-architecture machine. In the first example, the scan pattern of a simple block structure is designed. After measuring and comparing deformation of a block fabricated by initial and optimized scan pattern, it is found that the maximum upward bending after cutting off is reduced by 23% for the block structure after scan pattern optimization (i.e. reduced from 3.2 mm to 2.4 mm). This simple block structure shows the feasibility of scan pattern optimization to reduce residual deformation. The second example is a connecting rod with complex geometry. Similar to the first case, scan pattern of each island is optimized after voxelization. Build
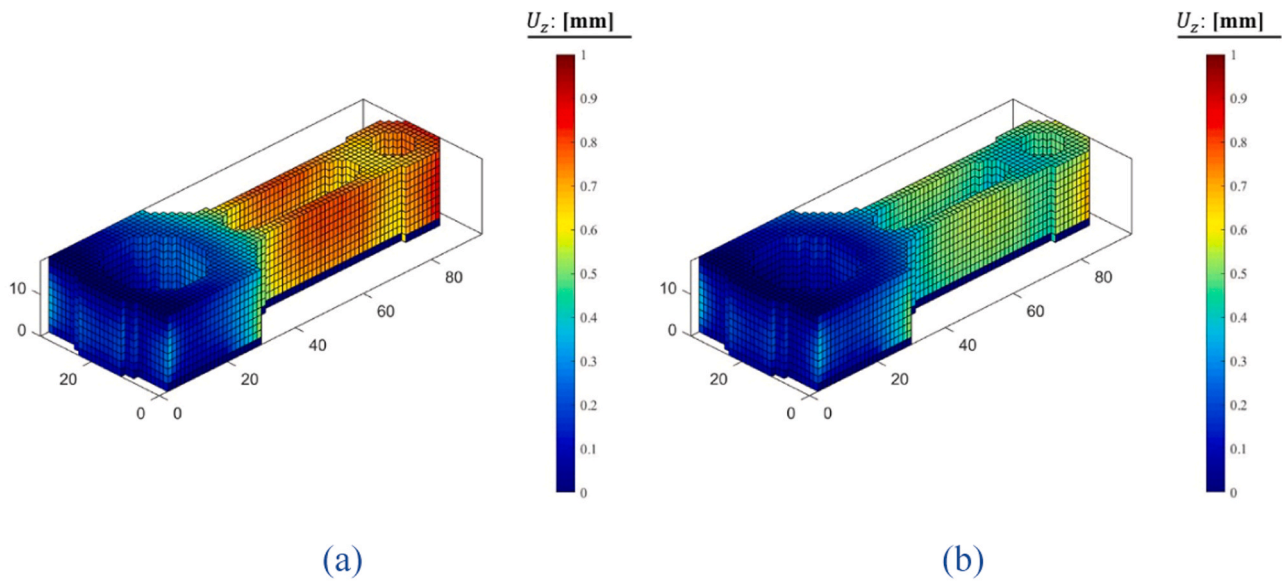
Fig. 15. Deformation profile under baseline scanning pattern (a) layer-wise 90° rotation and (b) neighboring island orthogonal and layer-wise 90° rotation.

Table 2
Deformation of connecting rod at tip point with different scanning pattern.

	Initial setup	Layer-wise rotation (90°)	Neighboring island orthogonal & layer-wise rotation (90°)	Optimized
U_z (mm)	0.83	0.83	0.53	0.45

path reconstruction is performed after optimization to compensate for the resolution lost (i.e. local geometric feature) in voxelization. The deformation of connecting rods built by the initial and optimized scan pattern is measured. The deformation comparison shows that the upward residual deformation near the tip region can be significantly reduced by ~50% after scanning pattern optimization.

For future work, high performance computing techniques such as GPU-based finite element analysis [52] could be employed to optimize the scan pattern of physical layers, instead of merged layers, for further residual deformation minimization. Layer-wise rotation or shift is usually employed in the real building process with island scanning strategy and has been reported to be effective in residual stress reduction. Layer-wise rotation angle and shifting distance can be another design variable to optimize as part of the future work. Although deformation comparison shows the effectiveness of this method, the accuracy of finite element analysis can still be improved by taking plasticity into consideration, which will make the sensitivity analysis much more challenging as well. In addition to residual deformation, the influence of optimized scanning patterns on microstructures, defects and build efficiency is also worth to investigate.

CRediT authorship contribution statement

Qian Chen: Conceptualization, Investigation, Methodology, Experiment, Simulation, Writing - original draft, Writing - review & editing. **Hunter Taylor**: Experiment, Writing - original draft. **Akihiro Takezawa**: Conceptualization, Investigation, Methodology, Editing. **Xuan Liang**: Experiment. **Xavier Jimenze**: Experiment. **Ryan Wicker**: Methodology, Supervision. **Albert C. To**: Conceptualization, Investigation, Methodology, Writing - original draft, Writing - review & editing.

Declaration of Competing Interest

The authors declare that they have no known competing financial interests or personal relationships that could have appeared to influence the work reported in this paper.

References

[1] H. Lei, C. Li, J. Meng, H. Zhou, Y. Liu, X. Zhang, P. Wang, D. Fang, Evaluation of compressive properties of SLM-fabricated multi-layer lattice structures by experimental test and μ-CT-based finite element analysis, Mater. Des. 169 (2019), 107685.

[2] C. Li, H. Lei, Z. Zhang, X. Zhang, H. Zhou, P. Wang, D. Fang, Architecture design of periodic truss-lattice cells for additive manufacturing, Addit. Manuf. 34 (2020), 101172.

[3] P. Kürnsteiner, M.B. Wilms, A. Weisheit, P. Barriobero-Vila, B. Gault, E.A. Jägle, D. Raabe, In-process precipitation during laser additive manufacturing investigated by atom probe tomography, Microsc. Microanal. 23 (S1) (2017) 694–695.

[4] E.R. Denlinger, J.C. Heigel, P. Michaleris, Residual stress and distortion modeling of electron beam direct manufacturing Ti-6Al-4V, J. Eng. Manuf. 229 (10) (2015) 1803–1813.

[5] L.H. Ahmed Hussein, Chunze Yan, Richard Everson, Finite element simulation of the temperature and stress fields in single layers built without-support in selective laser melting, Mater. Des. 52 (2013) 638–647.

[6] H. Ali, L. Ma, H. Ghadbeigi, K. Mumtaz, In-situ residual stress reduction, martensitic decomposition and mechanical properties enhancement through high temperature powder bed pre-heating of Selective Laser Melted Ti6Al4V, Mater. Sci. Eng. A 695 (2017) 211–220.

[7] M. Strantza, R.K. Ganeriwala, B. Clausen, T.Q. Phan, L.E. Levine, D. Pagan, W. E. King, N.E. Hodge, D.W. Brown, Coupled experimental and computational study of residual stresses in additively manufactured Ti-6Al-4V components, Mater. Lett. 231 (2018) 221–224.

[8] C. Knowles, T. Becker, R. Tait, Residual stress measurements and structural integrity implications for selective laser melted Ti-6Al-4V, S. Afr. J. Ind. Eng. 23 (3) (2012) 119–129.

[9] T. Simson, A. Emmel, A. Dwars, J. Böhm, Residual stress measurements on AISI 316L samples manufactured by selective laser melting, Addit. Manuf. 17 (2017) 183–189.

[10] W.E. King, A.T. Anderson, R.M. Ferencz, N.E. Hodge, C. Kamath, S.A. Khairallah, A.M. Rubenchik, Laser powder bed fusion additive manufacturing of metals; physics, computational, and materials challenges, Appl. Phys. Rev. 2 (4) (2015), 041304.

[11] J.L. Bartlett, X. Li, An overview of residual stresses in metal powder bed fusion, Addit. Manuf. 27 (2019) 131–149.

[12] P. Edwards, M. Ramulu, Fatigue performance evaluation of selective laser melted Ti–6Al–4V, Mater. Sci. Eng. A 598 (2014) 327–337.

[13] S. Leuders, M. Thöne, A. Riemer, T. Niendorf, T. Tröster, H.A. Richard, H.J. Maier, On the mechanical behaviour of titanium alloy TiAl6V4 manufactured by selective laser melting: fatigue resistance and crack growth performance, Int. J. Fatigue 48 (2013) 300–307.

[14] G.E. Totten, Handbook of Residual Stress and Deformation of Steel, ASM International, 2002.

[15] M. Baumers et al., Combined build-time, energy consumption and cost estimation for direct metal laser sintering, in: From Proceedings of Twenty Third Annual International Solid Freeform Fabrication Symposium—An Additive Manufacturing Conference, 2012.

[16] L. Cheng, et al., On utilizing topology optimization to design support structure to prevent residual stress induced build failure in laser powder bed metal additive manufacturing, Addit. Manuf. (2019).

[17] J.-P. Kruth, J. Deckers, E. Yasa, R. Wauthlé, Assessing and comparing influencing factors of residual stresses in selective laser melting using a novel analysis method, Proc. Inst. Mech. Eng. Part B J. Eng. Manuf. 226 (6) (2012) 980–991.

[18] L. Mugwagwa, D. Dimitrov, S. Matope, I. Yadroitsev, Evaluation of the impact of scanning strategies on residual stresses in selective laser melting, Int. J. Adv. Manuf. Technol. 102 (5) (2019) 2441–2450.

[19] J.-P. Kruth et al., Part and material properties in selective laser melting of metals, in: Proceedings of the 16th International Symposium on Electromachining, 2010.

[20] Y. Lu, S. Wu, Y. Gan, T. Huang, C. Yang, L. Junjie, J. Lin, Study on the microstructure, mechanical property and residual stress of SLM Inconel-718 alloy manufactured by differing island scanning strategy, Opt. Laser Technol. 75 (2015) 197–206.

[21] B. Cheng, S. Shrestha, K. Chou, Stress and deformation evaluations of scanning strategy effect in selective laser melting, Addit. Manuf. 12 (2016) 240–251.

[22] L. Thijs, K. Kempen, J.P. Kruth, J. Van Humbeeck, Fine-structured aluminium products with controllable texture by selective laser melting of pre-alloyed AlSi10Mg powder, Acta Mater. 61 (5) (2013) 1809–1819.

[23] X. Liang, W. Dong, Q. Chen, A.C. To, On incorporating scanning strategy effects into the modified inherent strain modeling framework for laser powder bed fusion, Addit. Manuf. 37 (2021) 101648.

[24] Q. Chen, J. Liu, X. Liang, A.C. To, A level-set based continuous scanning path optimization method for reducing residual stress and deformation in metal additive manufacturing, Comput. Methods Appl. Mech. Eng. 360 (2020), 112719.

[25] D. Ding, Z. Pan, D. Cuiuri, H. Li, A practical path planning methodology for wire and arc additive manufacturing of thin-walled structures, Robot. Comput. Integr. Manuf. 34 (2015) 8–19.

[26] D. Ding, Z. Pan, D. Cuiuri, H. Li, S. van Duin, N. Larkin, Bead modelling and implementation of adaptive MAT path in wire and arc additive manufacturing, Robot. Comput. Integr. Manuf. 39 (2016) 32–42.

[27] D.E. Smith, R. Hoglund, Continuous fiber angle topology optimization for polymer fused fillament fabrication, in: Annual International Solid Freeform Fabrication Symposium, Austin, TX, 2016.

[28] Q. Xia, T. Shi, Optimization of composite structures with continuous spatial variation of fiber angle through Shepard interpolation, Compos. Struct. 182 (2017) 273–282.

[29] C. Kiyono, E. Silva, J. Reddy, A novel fiber optimization method based on normal distribution function with continuously varying fiber path, Compos. Struct. 160 (2017) 503–515.

[30] C.J. Brampton, K.C. Wu, H.A. Kim, New optimization method for steered fiber composites using the level set method, Struct. Multidiscip. Optim. 52 (3) (2015) 493–505.

[31] J. Liu, H. Yu, Concurrent deposition path planning and structural topology optimization for additive manufacturing, Rapid Prototyp. J. 23 (5) (2017) 930–942.

[32] J. Liu, A.C. To, Deposition path planning-integrated structural topology optimization for 3D additive manufacturing subject to self-support constraint, Comput. Aided Des. 91 (2017) 27–45.

[33] H. Shen, J. Fu, Z. Chen, Y. Fan, Generation of offset surface for tool path in NC machining through level set methods, Int. J. Adv. Manuf. Technol. 46 (9–12) (2010) 1043–1047.

[34] C. Zhuang, Z. Xiong, H. Ding, High speed machining tool path generation for pockets using level sets, Int. J. Prod. Res. 48 (19) (2010) 5749–5766.

[35] E.R. Denlinger, J. Irwin, P. Michaleris, Thermomechanical modeling of additive manufacturing large parts, J. Manuf. Sci. Eng. 136 (6) (2014), 061007.

[36] E.R. Denlinger, M. Gouge, J. Irwin, P. Michaleris, Thermomechanical model development and in situ experimental validation of the Laser Powder-Bed Fusion process, Addit. Manuf. 16 (2017) 73–80.

[37] C. Seidel, M.F. Zaeh, M. Wunderer, J. Weirather, T.A. Krol, M. Ott, Simulation of the laser beam melting process–approaches for an efficient modelling of the beam-material interaction, Procedia CIRP 25 (2014) 146–153.

[38] C. Li, J. Liu, Y. Guo, Efficient predictive model of part distortion and residual stress in selective laser melting, in: Solid Freeform Fabrication 2016, 2017.

[39] P.Z. Qingcheng Yang, L. Cheng, Z. Min, M. Chyu, A.C. To, Finite element modeling and validation of thermomechanicalbehavior of Ti-6Al-4V in directed energy deposition additivemanufacturing. Addit. Manuf., 2016.

[40] H. Peng et al., Part-scale model for fast prediction of thermal distortion in DMLS additive manufacturing; Part 2: a quasi-static thermomechanical model.

[41] Y. Ueda, K. Fukuda, K. Nakacho, S. Endo, A new measuring method of residual stresses with the aid of finite element method and reliability of estimated values, J. Soc. Nav. Archit. Jpn. 1975 (138) (1975) 499–507.

[42] M. Yuan, Y. Ueda, Prediction of residual stresses in welded T-and I-joints using inherent strains, J. Eng. Mater. Technol. Trans. ASME 118 (2) (1996) 229–234.

[43] H. Murakawa, Y. Luo, Y. Ueda, Prediction of welding deformation and residual stress by elastic FEM based on inherent strain, J. Soc. Nav. Archit. Jpn. 1996 (180) (1996) 739–751.

[44] X. Liang, L. Cheng, Q. Chen, Q. Yang, A.C. To, A modified method for estimating inherent strains from detailed process simulation for fast residual distortion prediction of single-walled structures fabricated by directed energy deposition, Addit. Manuf. 23 (2018) 471–486.

[45] Q. Chen, X. Liang, D. Hayduke, J. Liu, L. Cheng, J. Oskin, R. Whitmore, A.C. To, An inherent strain based multiscale modeling framework for simulating part-scale residual deformation for direct metal laser sintering, Addit. Manuf. 28 (2019) 406–418.

[46] A.H. Tran, J.T. Flynn, R.C. Becker, S.R. Daniels, B.E. Falkner, M. Ferguson, C. D. Hanevold, S.R. Hooper, J.R. Ingelfinger, M.B. Lande, L.J. Martin, K. Meyers, M. Mitsnefes, B. Rosner, J.A. Samuels, E.M. Urbina, Subclinical systolic and diastolic dysfunction is evident in youth with elevated blood pressure, Hypertension 75 (2020) 1551–1556.

[47] H.T. Tran, X. Liang, A.C. To, Efficient prediction of cracking at solid-lattice support interface during laser powder bed fusion via global-local J-integral analysis based on modified inherent strain method and lattice support homogenization, Addit. Manuf. 36 (2020), 101590.

[48] L. Cheng, A. To, Part-scale build orientation optimization for minimizing residual stress and support volume for metal additive manufacturing: theory and experimental validation, Comput. Aided Des. 113 (2019) 1–23.

[49] J. Gao, M. Xiao, Y. Zhang, L. Gao, A comprehensive review of isogeometric topology optimization: methods, applications and prospects, Chin. J. Mech. Eng. 33 (1) (2020) 1–14.

[50] J. Gao, M. Xiao, L. Gao, J. Yan, W. Yan, Isogeometric topology optimization for computational design of re-entrant and chiral auxetic composites, Comput. Methods Appl. Mech. Eng. 362 (2020), 112876.

[51] A. Takezawa, A.C. To, Q. Chen, X. Liang, F. Dugast, X. Zhang, M. Kitamura, Sensitivity analysis and lattice density optimization for sequential inherent strain method used in additive manufacturing process, Comput. Methods Appl. Mech. Eng. 370 (2020), 113231.

[52] F. Dugast, P. Apostolou, A. Fernandez, W. Dong, Q. Chen, S. Strayer, R. Wicker, A. C. To, Part-scale thermal process modeling for laser powder bed fusion with matrix-free method and GPU computing, Addit. Manuf. 37 (2021), 101732.